Imaging current control of magnetization in Fe 3 GeTe 2 with a widefield nitrogen-vacancy microscope

Islay O Robertson, Cheng Tan, Sam C Scholten, Alexander J Healey, Gabriel J Abrahams, Guolin Zheng, Aurélien Manchon, Lan Wang, Jean-Philippe Tetienne

Imaging current control of magnetization in Fe_3GeTe_2 with a widefield nitrogen-vacancy microscope

Islay O. Robertson,[1,2] Cheng Tan,[1] Sam C. Scholten,[2,3] Alexander J. Healey,[2,3] Gabriel J. Abrahams,[1,2] Guolin Zheng,[1] Aurélien Manchon,[4] Lan Wang,[1] and Jean-Philippe Tetienne[1,*]

[1] *School of Science, RMIT University, Melbourne, VIC 3001, Australia*
[2] *School of Physics, University of Melbourne, VIC 3010, Australia*
[3] *Centre for Quantum Computation and Communication Technology, School of Physics, University of Melbourne, VIC 3010, Australia*
[4] *CINaM, Aix-Marseille Université, CNRS, Marseille, France*

Van der Waals (vdW) magnets are appealing candidates for realising spintronic devices that exploit current control of magnetization (e.g. switching or domain wall motion), but so far experimental demonstrations have been sparse, in part because of challenges associated with imaging the magnetization in these systems. Widefield nitrogen-vacancy (NV) microscopy allows rapid, quantitative magnetic imaging across entire vdW flakes, ideal for capturing changes in the micromagnetic structure due to an electric current. Here we use a widefield NV microscope to study the effect of current injection in thin flakes ($\sim 10\,\mathrm{nm}$) of the vdW ferromagnet Fe_3GeTe_2 (FGT). We first observe current-reduced coercivity on an individual domain level, where current injection in FGT causes substantial reduction in the magnetic field required to locally reverse the magnetisation. We then explore the possibility of current-induced domain-wall motion, and provide preliminary evidence for such a motion under relatively low current densities, suggesting the existence of strong current-induced torques in our devices. Our results illustrate the applicability of widefield NV microscopy to imaging spintronic phenomena in vdW magnets, highlight the possibility of efficient magnetization control by direct current injection without assistance from an adjacent conductor, and motivate further investigations of the effect of currents in FGT and other vdW magnets.

I. INTRODUCTION

Exfoliation of two-dimensional (2D) van der Waals (vdW) magnets has created opportunities for developing new methods for integrating magnetic materials into future and existing technologies.[1] Their low dimensionality favours the use of weak external stimuli such as strain, electric fields, or low-power currents to alter or interact with the micromagnetic structure.[2,3] Furthermore, their freestanding nature facilitates stacking layers of material at different angles to create twisted structures or layering with different materials (heterostructures) to create new interface interactions.[4,5] Exploiting external stimuli and interface interactions are driving the development of new devices based on vdW magnets.[5–11] An area of significant interest for 2D vdW magnets is spintronics, where external stimulation and interface interactions play an important role in creating a variety of phenomena,[11–14] which primarily involve the interaction between the magnetic structure of a host material and the magnetic moment of injected electrons. Current injection will generally either alter the behaviour of the injected electrons, or induce changes in the micromagnetic structure of the host material. A particular phenomenon which changes the domain structure of the host magnetic material is current-induced domain-wall motion (CIDM) where the injection of currents into the material (or in an adjacent conductor) causes growth/shrinkage of adjacent magnetic domains thereby moving the domain wall separating them,[15–17] which can be extended to more complex magnetic textures such as skyrmions.[18] Significant interest in CIDM is primarily due to the mechanisms driving the motion, namely the spin-transfer torque (STT) and spin-orbit torque (SOT) which are often studied in conventional magnetic multilayer systems for potential applications in future highly efficient magnetic memory and logic devices.[14] Note that while such multilayer systems are generally ferromagnetic with perpendicular magnetic anisotropy, antiferromagnets, synthetic or intrinsic, can be more efficient for CIDM than their ferromagnetic counterparts due to the absence of stray fields stabilizing adjacent domains, however, this also makes them exceptionally difficult to study.[14] Identification of SOTs in vdW systems offers new pathways for engineering devices with the potential for even greater efficiencies.[19,20] While magnetization switching by SOT has been achieved in various 2D or hybrid 2D/3D systems,[21–24] so far CIDM has not been observed in vdW structures.[25]

Commonly, spintronic phenomena are inferred from transport measurements, which give little insight into the micromagnetic structure as they offer no means of direct observation of the material.[26] To fully understand changes in the domains, e.g. to unambiguously identify CIDM, high resolution magnetic imaging techniques need to be employed. Magnetic imaging is most often applied to the study of 2D vdW magnets using scanning probe techniques and magneto-optical effects. Scanning probe techniques, e.g. based on single nitrogen-vacancy (NV) centers in diamond, often yield the highest spatial resolution at the cost of longer image collection times and smaller fields of view, limiting images to small sections of the subject material.[27] Magneto-optical methods based on the Kerr effect and magnetic circular dichroism are capable of larger fields of view but materials must

facilitate the necessary optical interactions and require careful calibration to make quantitative measurements.[26] Such restrictions can inhibit the study of spintronic phenomena by preventing quantitative analysis and limiting studies to certain materials or designated regions. To compensate for some of the shortcomings of preexisting magnetic imaging techniques, here we utilise widefield NV microscopy[28,29] as a method for imaging 2D vdW magnets, by optically probing magnetic stray fields from a sample material via a proximal, dense layer of NV centers. Widefield NV microscopy, also known as quantum diamond microscopy, offers calibration-free quantitative imaging with sub-micrometer resolution over a comparatively large field of view, and high measurement throughput, properties which suitably lend themselves to systematically studying the micromagnetic structure across the full surface of 2D vdW magnets, as demonstrated recently by several groups.[30–32] Similarly, these features are also desirable for imaging spintronic phenomena,[33] but the technique is yet to be applied to vdW spintronic devices. Here, we apply widefield NV microscopy to studying current-induced changes in the micromagnetic structure of a 2D vdW ferromagnet using Fe_3GeTe_2 (FGT)[34–37] as the host material.

FGT stands out amongst other vdW magnets as it is a ferromagnetic metal with large anomalous Hall conductance[38] which, along with its conductivity and relatively high Curie temperature ($\approx 200\,\mathrm{K}$[35]), makes it ideal for studying spintronic phenomena. Additionally, its crystal symmetry supports strong spin-orbit coupling which can stabilise chiral spin structures and skyrmions.[39–41] A number of current-induced spintronic effects have been identified in FGT including: current-reduced coercivity,[9] antisymmetric magnetoresistance,[8] bilayer-assisted magnetization switching,[21,22,24] and skyrmion motion.[42] Here, we aim to study the possibility of CIDM in FGT thin flakes when the current is injected directly into the FGT layer, without assistance from an adjacent conductive layer. Our study was inspired by recent works[9,43,44] which suggested an efficient bulk SOT in FGT by direct current injection, an intriguing departure from the bilayer systems mainly studied so far, in which the current flows in a non-magnetic conductor creating an interfacial SOT acting on the adjacent ferromagnet.[14,16,17,21–24] We first use our microscope to characterise FGT flakes without electrodes, and highlight the requirements for imaging contacted FGT devices. We then image such a device, observe a local reduction in coercivity due to current pulses, and suggest some ideal conditions for observing CIDM. Finally we provide the evidence of CIDM in a separate FGT device, at relatively low current densities. The possible nature of the magnetisation dynamics and role of current-induced torques (e.g. SOT) are discussed. Our results suggest the possibility of efficient control of the magnetic microstructure of thin FGT flakes by direct current injection, and motivate further investigations of the effect of currents in FGT and other vdW magnets. They also illustrate the applicability, and associated challenges, of widefield NV microscopy to imaging spintronic phenomena in vdW magnets.

II. RESULTS AND DISCUSSION

Widefield NV microscopy employs a diamond sensor which is interfaced with the sample of interest,[29] in this instance a contacted spintronic device [Fig. 1(a)]. The sensor is composed of a shallow layer of magnetically sensitive NVs embedded in the diamond lattice whose ground state spin transitions are influenced by stray fields emanating from a proximal magnetic material such as FGT [Fig. 1(b)]. Illuminating the NV layer with a green (532 nm) laser, coupled with microwave excitation, probes the NV spin transitions which are then readout by their red photoluminesence in a process known as optically detected magnetic resonance (ODMR).[45–47] To study spintronic phenomena, we constructed devices by exfoliating flakes of FGT (thickness $\sim 10\,\mathrm{nm}$) and transferring them onto platinum contacts which were fabricated on a silicon substrate and then wire-bonded to an external power source. The device is mounted on a printed circuit board which contains a coplanar microwave waveguide for driving the NVs' spin transitions [Fig. 1(c)]. A diamond is then placed onto the surface of the device in such a way to ensure the NV layer is in close contact with the flake of FGT [Fig. 1(d)] (method in SI, Sec. III). The FGT flake bridges a number of contacts [Fig. 1(e)] and is coated with a protective layer to limit atmospheric exposure (details in SI, Sec. II).

An example magnetic image for the device in Fig. 1(e) taken with the widefield NV microscope shows magnetic fields emanating almost exclusively from the outlined flakes of FGT [Fig. 1(f)]. The image is generated by simultaneously recording ODMR spectra at each pixel on a camera. To extract stray field information from the ODMR spectra, images are taken under a bias field ($B^0_{\mathrm{NV}} = 6\,\mathrm{mT}$) applied along a particular NV axis creating two ODMR peaks separated by $\Delta f = 2\gamma_e(B^0_{\mathrm{NV}} + B_{\mathrm{NV}})$ where $\gamma_e \approx 28\,\mathrm{GHz\,T^{-1}}$ is the electron gyromagnetic ratio.[46] In this way the projection of the stray field from the material along the specified NV axis (B_{NV}) can be recovered.[29] We collect our magnetic images using a custom-built widefield microscope system constructed around a cryogenic chamber[48] to facilitate imaging below the Curie temperature of FGT. Except in Fig. 2, the diamond crystal orientation is chosen so the projection axis coincides with the out-of-plane (z) axis, i.e. $B_{\mathrm{NV}} = B_z$. Given FGT is magnetized out of plane due to perpendicular magnetic anisotropy,[35] there is a relatively simple correspondence between measured stray field and underlying magnetization, as illustrated in Fig. 1(b), which facilitates visualisation of magnetic domains.

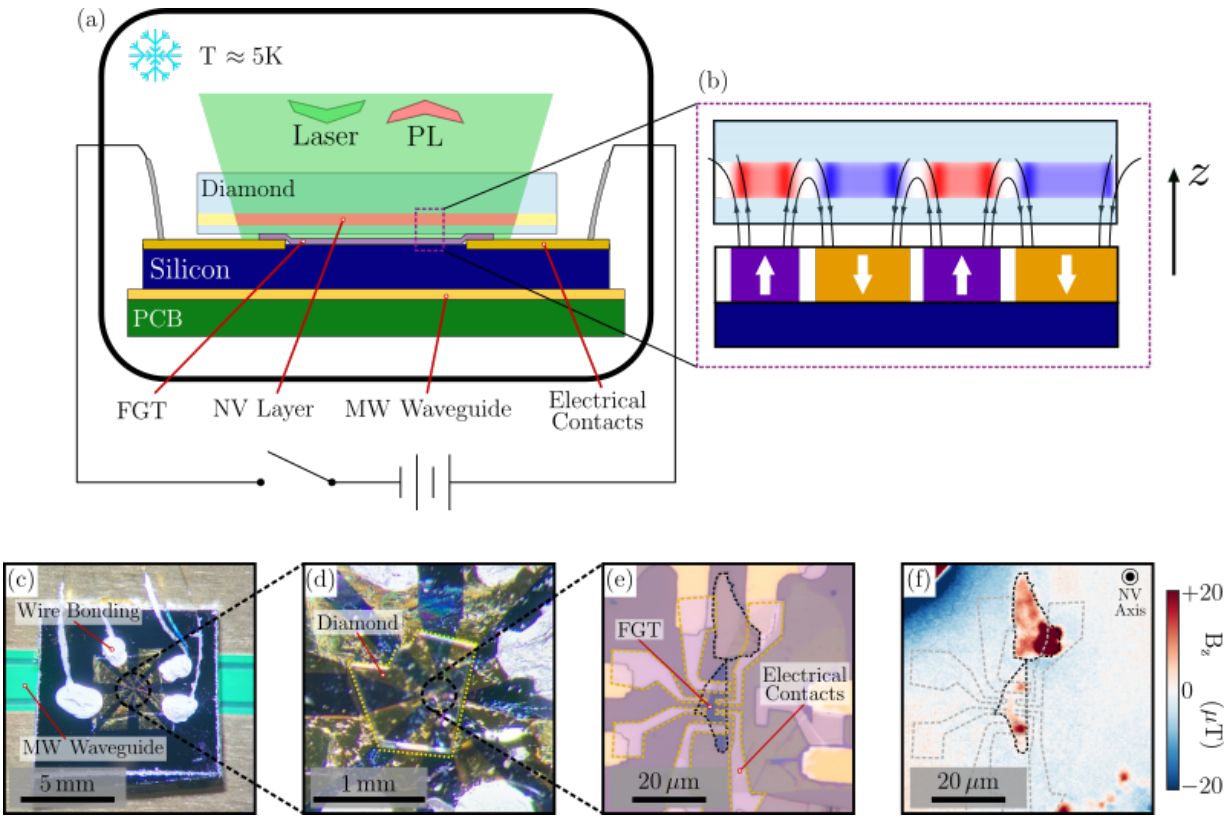

FIG. 1. **Imaging spintronic devices with widefield NV microscopy.** (a) Cross-sectional schematic of a spintronic device with a surface mounted diamond containing a shallow nitrogen-vacancy (NV) layer. The device centrepiece is a thin flake of Fe_3GeTe_2 (FGT), a van der Waals magnet which conforms to the silicon substrate/electrical contact topography. The device is placed on a printed circuit board (PCB) with a microwave (MW) waveguide for driving the NV spin resonances. For measurement the entire device is placed in a cryogenic chamber with a base temperature of $\approx 5\,\mathrm{K}$. (b) Stray fields from the domain structure are mapped by optically interrogating the array of NVs which act as local magnetometers. In this way a map of the stray field at the NV layer is measured. (c) Optical image of an example spintronic device mounted on a circuit board and connected to a power source via wire bonding for current injection. (d) Optical micrograph of the device in (c) with a diamond mounted on top. The diamond is glued at its corners to ensure it remains in place when loading into the cryostat to help maintain close proximity to the device. (e) Optical micrograph at the centre of the spintronic device (taken prior to diamond mounting) showing flakes of FGT (black contours) positioned over platinum contacts (yellow contours). (f) Stray field image of the device in (e) obtained with widefield NV microscopy, recorded under a bias field $B^0_{\mathrm{NV}} = 6\,\mathrm{mT}$ applied along the NV axis coinciding with the z axis. Prior to imaging, the device was heated to near the Curie temperature and then cooled under the 6 mT field.

Characterisation of isolated FGT flakes

As a first step towards CIDM, we characterised the ferromagnetic properties of isolated FGT flakes (i.e. without electrical contacts) using the widefield NV microscope. In this way we can build an understanding of the conditions under which we will be trying to move domain walls. For this characterisation, flakes of FGT were exfoliated from bulk material and transferred directly onto the surface of a diamond [Fig. 2(a)]. Doing so allows us to probe field and temperature dependence of the magnetic properties with optically limited spatial resolution.[30] Under a bias field of 6 mT, we first image FGT flakes at 5 K, immediately after bringing them below the Curie temperature with a null external field (zero-field cooled). Upon zero-field cooling, ferromagnetic materials tends to minimise the free energy by forming disorganised domain structures which lead to a net-zero stray field. Our stray-field image [Fig. 2(b)] is consistent with this prediction as we observe regions of net-zero stray field at the interior of the flakes where the domains are below the spatial resolution ($\approx 700\,\mathrm{nm}$[48]). Larger domain features which are above the spatial resolution are located along the edges.

Starting from this virgin state, we study the magnetization dynamics by taking a series of images between the application of incrementally increasing magnetic fields along the magnetic easy axis (z axis) of FGT [Fig. 2(c)]. The disorganised domain structure is removed as the strength of the applied field is increased and the flake becomes comprised of a single domain aligned parallel to the direction of the applied field. The delayed transition to a fully magnetised structure suggests domain

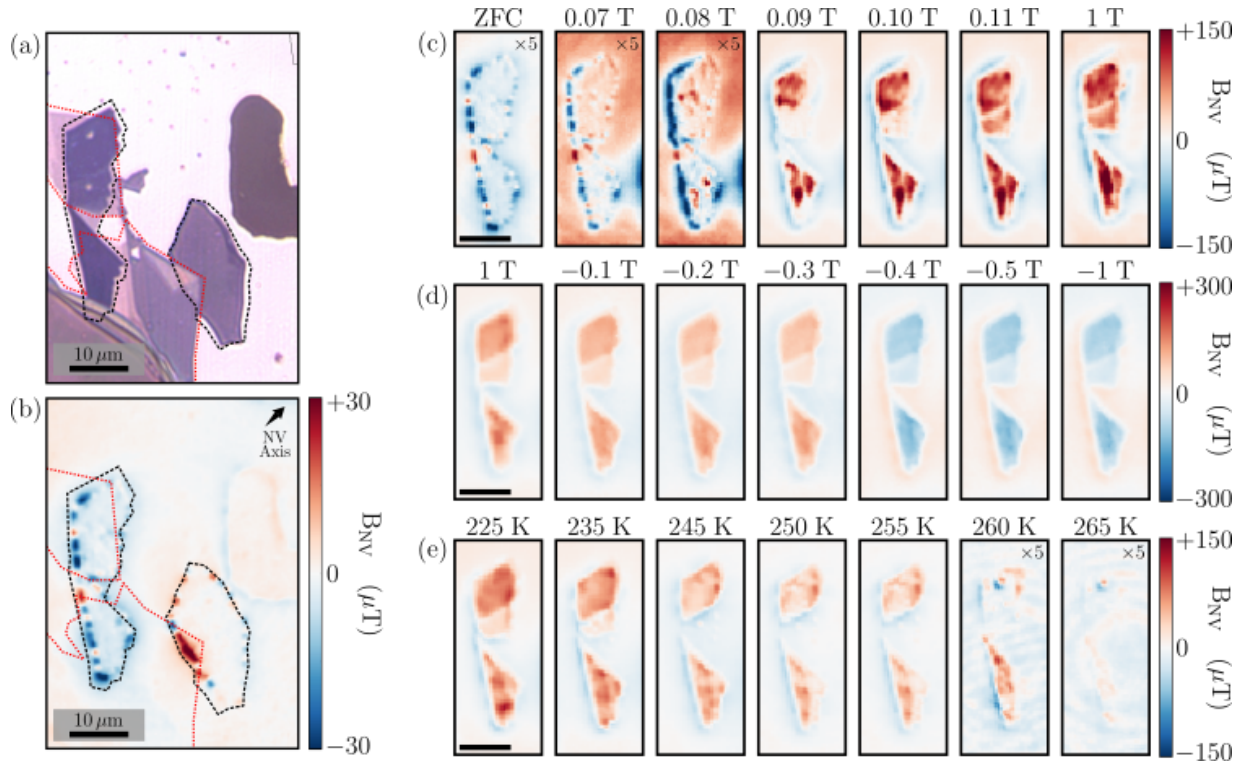

FIG. 2. **Imaging the ferromagnetic properties of FGT flakes.** (a) Flakes of FGT (black outline) (maximum thickness 18 nm or 23 layers) on the surface of an Al-coated diamond. FGT is placed on top of flakes of WTe_2 (red outline) (≈ 3 nm or 3 layers) with partial overlap with FGT forming heterostructures locally. The features not outlined are registration marks made in the Al coating. (b) Stray-field image of the FGT flakes after zero field cooling, recorded under a bias field $B^0_{\mathrm{NV}} = 6$ mT applied along the NV axis (direction indicated by the arrow in the top-right corner, pointing 55° off the z axis). (c-e) Stray-field image series for probing the depinning field c), switching field d), and temperature dependent phase transition e) in FGT for one of the flakes in a). (c) To measure the depinning field, the series starts from the zero-field-cooled state and then images are taken after fields of increasing magnitude are applied along the easy axis of magnetization (z axis) until the flake is observed to be fully magnetized (≈ 0.11 T). (d) For the switching field, fields of increasing magnitude are applied in opposition to a positive single domain state until there is a reversal of polarity in the stray field. (e) The temperature dependent phase transition can be studied by imaging under increasing temperatures. Starting at 225 K the temperature is increased until stray fields are no longer observed from the flake at 265 K. All images are taken under a bias field $B^0_{\mathrm{NV}} = 6$ mT.

walls are pinned within the flake creating an energy barrier to domain growth. Thicker (≈ 18 nm) sections form a single domain after the application of 0.08 T while the thinner sections (≈ 8 nm or 10 layers) require 0.11 T. Following this, the maximum field strength is applied (1 T), resulting in minimal change to the magnetization, thus we infer the flake had already been magnetised at this stage. These quantitative magnetic field maps can be used to reconstruct the out-of-plane magnetization map (M_z) using a Fourier inversion method.[27,30,49] For the fully magnetised case in Fig. 2(c), we find an areal magnetization density ranging between 20 and 50 $\mu_{\mathrm{B}}\,\mathrm{nm}^{-2}$, which is over an order of magnitude less than expected from the known magnetization of bulk FGT (see SI, Sec. VI); the reason for this weak magnetization in our thin flake samples is currently not understood. With a fully magnetised flake, we similarly take a series of images between the application of fields with increasing strength in opposition to the magnetization to try and reverse the polarity of the flake [Fig. 2(d)]. Reversal occurs after applying −0.4 T reaffirming previously reported hard ferromagnetic properties,[35] with no visible thickness dependence.

Again starting from a fully magnetised state, a series of magnetic field images can be taken at increasingly higher temperatures to find the critical temperature at which ferromagnetic order is lost [Fig. 2(e)]. Here we once again observe a separate behaviour in different sections of the flake; the thinner region becomes demagnetised at a lower temperature (245 K) than the rest of the flake (265 K). Note, our system overestimates the flake's temperature due to separation between the heating element/readout and the FGT sample.[30]

Being able to reliably control domain nucleation in precise locations within the flake is a necessary part of studying CIDM. However, the formation of domains under the application of magnetic fields and temperatures to magnetised and demagnetised flakes of FGT [Fig. 2(c-e)] leads to disorganised structures which is unreliable when trying to repeatably force domains in the same location

for repetitive studies of the effect of current injection. By visualising the domain structure we can see Fig. 2(b) suggests domain pinning may be facilitated by strain within the FGT structure; indeed a correlation can be observed between the domain structure (following zero-field cooling) and the border of flakes located underneath the FGT (WTe_2 flakes in this case, outlined in red in Fig. 2(a)), resulting from external pressure at points of overlap. Thus, local topography features may be used as a way to nucleate domain walls in a reproducible fashion, as required for CIDM studies. We note the WTe_2 layer has no observable impact on the magnetic behaviour of FGT studied in Fig. 2(c-e) otherwise.

Observation of current-reduced coercivity

To first demonstrate imaging spintronic effects, we consider current-reduced coercivity, a phenomenon previously observed in FGT and reported to arise from bulk SOTs generated by the injection of currents directly in the FGT flake.[9,10] SOTs are supported in FGT by the broken inversion symmetry within its crystal structure.[43,44] We study this effect by constructing a device with a flake of FGT placed between two electrical contacts [Fig. 3(a)] and taking an image series in a similar fashion to measuring the switching field in Fig. 2(d), at 5 K. We first start by magnetizing the flake with a strong field (1 T) along the z-axis. Smaller fields are then applied in the opposite direction and a current is injected by applying a short (100 ns) voltage pulse across the two contacts [Fig. 3(b)]. The field is incrementally increased until the magnetization is reversed. We repeat this process for different voltage pulses. During image collection the field strength is reduced to 6 mT.

The image series depicts how as the strength of the voltage pulse is increased, the field required for switching the magnetization is reduced [Fig. 3(c)]. For no applied voltage (0 V), switching occurs across the entire flake at approximately the same field expected from our previous switching field measurement (−0.3 T here). When applying a 2 V pulse, we can now see a reduction in the stray-field emanating from a portion of the flake at −0.2 T. Under the same field, if a 3 V pulse is applied, the stray field in the same portion fully reversed. Further increasing the voltage (up to 7 V) reduces the field required for switching and increases the area affected. Note with a 2 V pulse, the magnetization is not fully reversed as the magnitude of the switching field is close to the current-free switching field. Thus we confirm increasing the voltage leads to a decrease in the coercive field.

Interestingly, wide-field NV microscopy enables the observation of current-assisted switching occurring in only a portion of the flake, which we show more clearly with an enlarged image in Fig. 3(d). In fact the areas where switching does not occur only switch when the 0 V switching field of −0.3 T is applied [see SI, Sec. VII]. The localisation of the reduced coercivity effect suggests the reduction occurs in an area of sufficient current density through the FGT. Considering the portion of the flake visibly affected by the current, we can construct a phase diagram by plotting the measured stray field emanating from the flake as a function of the applied field and magnitude of the voltage pulse [Fig. 3(e)], highlighting the dependence of the coercive field (H_c) on the magnitude of the applied voltage (black dotted line). To facilitate analysis, H_c is plotted against the current density, determined from low-current measurements of the resistance and an estimated cross-sectional area of $\approx 0.1\,\mu m^2$, and fit with a linear relationship [Fig. 3(f)]. For a maximum injected current density of $10^{10}\,A\,m^{-2}$ (7 V) we observe a 96% reduction in the coercive field which is within the range of the $50-100\%$ reduction at similar current densities reported in Ref..[9]

The reduced coercivity effect is understood to arise from both Joule heating and SOT.[9] Joule heating raises the temperature of the FGT, bringing it closer to the ferromagnetic phase transition which softens the characteristically hard magnetic behaviour. Simplistically, the Joule heating effect is expected to increase in strength while raising the magnitude of the voltage pulse as further heating is induced. SOT lowers the energy barrier for magnetization reversal with an effective field H_{SOT}, generated by spin-orbit coupling between the injected electrons and the orbital structure of FGT. The effective field acts on the native magnetic moments and destabilises the magnetization, subsequently reducing the field required for switching.[9] We can approximate the contribution of the SOT to the reduced coercivity effect in the low current regime using the relationship $H_c(0) - H_c(J) \approx H_{SOT}$.[50] We find a slope of $H_{SOT} \approx 30\,mT$ per $10^9\,A\,m^{-2}$ which to an order of magnitude is consistent with previous measurements.[9] Note, this is an overestimation of H_{SOT} as we do not thoroughly account for Joule heating, which could be responsible for up to 60% of the effect in this sample at $J = 10^{10}\,A\,m^{-2}$.[9]

Observation of current-induced domain wall motion

While imaging the current-reduced coercivity, we also tested whether CIDM could be produced in this device, i.e. whether the domain structure can be altered by a current in the absence of magnetic field. However no effect resembling CIDM was able to be observed. We believe this to be due to a sub-optimal device structure as the comparatively large contacts on a small flake of FGT make the nucleation of appropriately sized domains more difficult and decreases the length scale over which we can observe domain-wall motion. Thus, we next studied a spintronic device constructed using the same methods as the device in Fig. 3(a), but now with multiple, smaller electrical contacts [Fig. 4(a)]. Prior to current injection, we image the zero-field-cooled state to use as a reference for proceeding images, with barely visible domains close to our spatial resolution [Fig. 4(b)]. Currents are sup-

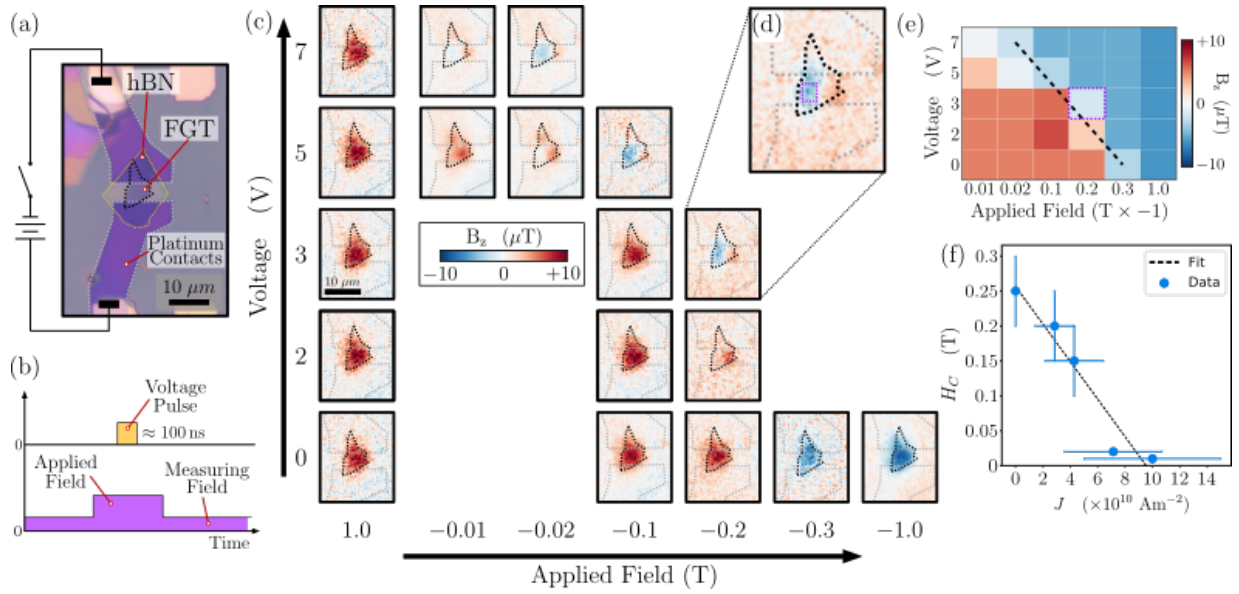

FIG. 3. **Imaging of current-reduced coercivity in FGT**. (a) Spintronic device fashioned from a flake of FGT (≈ 8 nm or 10 atomic layers), capped with a protective hexagonal boron nitride (hBN) layer, resting on platinum contacts which connect to an external power source. The diamond sensor (not shown here) was placed on top like in Fig. 1(d). (b) To manipulate the coercive field, short voltage pulses are injected into the FGT while a strong variable field is applied along the easy axis (z axis). The field is then reduced to $B^0_{\mathrm{NV}} = 6\,\mathrm{mT}$ for imaging (here the NV axis coincides with the z axis). (c) Series of magnetic stray-field images taken with voltage pulses of increasing strength injected under various external magnetic fields. As the applied voltage is increased the field for switching the magnetization decreases. (d) Magnified stray-field image showing the reduced coercivity effect is localised to a particular region of the flake (purple) between the two electrical contacts (grey). (e) Phase diagram of the stray field measured at the sampled location highlighted in d), indicative of domain polarity, as a function of the applied voltage pulse and the applied magnetic field. Dotted line is a guide to the eye representing polarity switching. (f) Coercive field (H_c) estimated from the phase diagram in e) plotted against the estimated current density (J). A linear fit (dotted line) allows for estimating the spin torque efficiency. Error bars in the coercive field and current density correspond to the step size in the applied field and the uncertainty in estimating the cross-sectional area, respectively.

plied to the flake of FGT by connecting two of the contacts (highlighted in yellow) to an external power source, and are injected while the small (6 mT) bias field is applied along the z-axis [Fig. 4(c)]. After current injection the magnetic stray field is imaged to determine whether it has resulted in a change in the domain structure. Taking a series of images after injecting currents of both increasing magnitude and in alternating directions [Fig. 4(d)], we observe the growth of domains between the two contacts with polarity both aligned and in opposition to the constant bias field.

Namely, starting from the zero-field-cooled state, a +0.1 mA current is briefly ($\sim$ 1 s) applied to the unmagnetised flake. The resulting micromagnetic structure shows little deviation from the zero-field-cooled state suggesting the supplied current is insufficient to overcome the energy barrier to drive domain wall motion.[51] At this stage, small domains of positive (red, i.e. pointing towards $+z$) and negative (blue, $-z$) polarity are visible near the left and right contacts, respectively, with a large white domain in between, indicating there are at least 3 domain walls between the contacts. Increasing the current to +0.2 mA leads to the growth of a singular domain (red, $+z$ polarity) between the contacts. Reversing the direction of the current at this value leads to no significant change in the domain structure [see full image series in SI, Sec. VII]. Further increasing the current to +0.3 mA leads to the growth of a new domain with the opposite polarity (blue, $-z$) to the previous domain. By changing the direction of the current the domain is shrunk by growing an adjacent opposing ($+z$) domain. The growing (shrinking) of domains after the injection of currents suggests the current is pushing a domain wall through the flake of FGT. As the bias field is present during the current injection (pointing towards $+z$), we can rule out trivial current-reduced coercivity or thermal effects, both of which would exclusively lead to domain growth with positive polarity, in alignment with the bias field. We also note domains external to the two electrical contacts remain unchanged throughout. Considering the injection of ±0.3 mA, we suggest the positive current has pushed a domain wall from left to right before the negative current then pushes it back (right to left) [Fig. 4(e)]. Consequently, the domain wall is determined to be moving against the direction of conventional current.

CIDM in metallic nano-wires and multilayer structures is generally attributed to two driving mechanisms, STT and SOT.[15,16] In each case, a spin current is generated

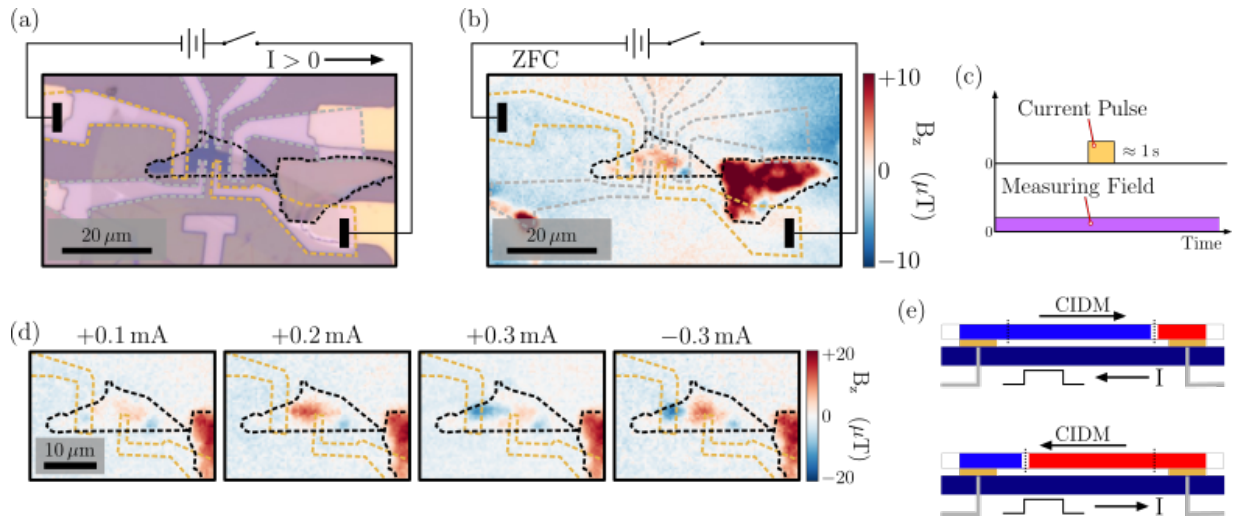

FIG. 4. **Imaging of current-induced domain wall motion in FGT**. (a) Spintronic device composed of multiple platinum electrical contacts with a flake of FGT (≈ 12 nm or 15 atomic layers) positioned on top. We connect our power supply to only two of the contacts (highlighted in yellow). This is the same device as shown in Fig. 1(c-f) (images were rotated), with the diamond sensor mounting shown in Fig. 1(d). (b) Corresponding magnetic image of the zero-field-cooled state prior to any current injection. (c) Current pulses are injected while a small measuring field ($B^0_{\mathrm{NV}} = 6$ mT applied along the z axis) is being applied. (d) Magnetic images are taken after currents of increasing magnitude are injected. +0.2 mA results in the growth of a domain between the two contacts. Subsequent injection of +0.3 mA results in growth of a new domain of opposite polarity which then shrinks after injecting a current in the opposite direction. (e) A schematic representation of current-induced domain wall motion (CIDM) describing the events resulting in the images taken after the injection of ±0.3 mA respectively. The domain walls move in opposition to conventional current.

by polarising the magnetic moments of the injected electrons. For STT, the current is polarised when passing through the magnetic material, a torque is then generated by an effective magnetic field which acts upon the domain wall. In the case of SOTs, spin polarisation arises from spin-orbit coupling, generally in an adjacent nonmagnetic layer. Similar to STT, the spin current generates an effective field which creates a torque at the domain wall. Both torques act on the local magnetic moment within the domain wall forcing it to move in a direction dependent on the polarity of the spin current and the domain wall geometry.[14] To characterise the spin torque efficiency (regardless of its type and origin) in CIDM experiments, it is common to consider the equivalent magnetic field needed to be applied to move the domain wall. Here, the depinning field is at least 6 mT, the value of the bias field. If we assume our device has a cross-sectional area of $\approx 0.1\,\mu\mathrm{m}^2$ and consider the case where 0.3 mA is applied to grow a domain opposed to the bias field, i.e. the current needs to be equivalent to a −12 mT applied field at least, we find a spin-torque efficiency of 4 mT per $10^9\,\mathrm{A\,m^{-2}}$. This is nearly two orders of magnitude more efficient than in conventional multilayer systems with perpendicular magnetic anisotropy such as Pt/Co/AlO_x and Ta/CoFe/MgO[15,16] and is similarly also more efficient than in synthetic antiferromagnetic systems.[52] In these systems, SOT arising from the spin Hall effect in the heavy metal underlayer is believed to be the dominant mechanism.[14,16]

The reason for the high spin-torque efficiency observed in our experiments may be due to the bulk SOT generated by the spin Hall effect, in contrast to the interfacial SOT at play in multilayer systems. The existence of bulk SOT in FGT was recently confirmed by transport measurements using harmonic analysis, with effective fields of up to 0.5 mT per $10^9\,\mathrm{A\,m^{-2}}$ reported,[44] which compares favourably to our value determined above. However, the existence of a spin torque does not guarantee domain wall motion,[14] and the exact mechanism driving CIDM in our experiments remains unclear. Using symmetry arguments based on the D_{3h} point group of monolayer FGT[53,54] [see SI, Sec. X], it is found the chiral spin spirals typically associated with SOT-driven domain-wall motion are not stabilized, suggesting there may be additional unexplored mechanisms contributing to the observed behaviour. Possible mechanisms responsible for CIDM in FGT may involve interfacial effects, strain, material defects or interlayer interactions (within FGT). Even in ideal FGT, current-induced torques is still a subject of intense research[44] as illustrated by the recent description of the so-called orbital torque.[55] A study of the effect of these current-induced torques on domains walls in ideal and real samples is beyond the scope of the present work. Thermal effects may also play a nontrivial conflating role.

Further studies of CIDM in this particular device were prevented after excessive Joule heating caused the device to fail [see SI, Sec. IX], when raising the current

above 0.3 mA. Subsequent FGT devices we have tested have shown reproducibility of the CIDM effect is in part dependent on device structure, including: electrical contact structure, electrical contact placement, and flake size. For future studies the current-reduced coercivity behaviour could be exploited to reliably nucleate domains at precise locations. Such amendments will enable more thorough and systematic studies of CIDM with widefield NV microscopy, which will help inform theoretical studies of the underlying mechanisms.

III. CONCLUSIONS

In this work, we resolved the entire micromagnetic structure of thin flakes of FGT using widefield NV microscopy to enable the study of spintronic phenomena, namely current-reduced coercivity and current-induced domain wall motion. We have respectively confirmed and demonstrated how the existence of efficient current-induced torques enables low power control of the magnetic domains, a desirable feature for future 2D vdW magnet devices. However, the preliminary study of the ferromagnetic properties demonstrate potential challenges for future studies and device implementation. The working temperature of FGT based devices has to be below room temperature to facilitate the critical behaviour of ferromagnetism and, reliable nucleation of domains within a flake of material requires an external force such as strain. Ionic gating and integration with topological insulators have been shown to raise the Curie temperature of FGT[37,56] as has increasing the iron content.[57] Controlling the nucleation of domains is likely better facilitated by the current-reduced coercivity phenomenon which we have shown to only affect areas of the flake with significant current flow. The bulk SOT native to FGT, which is responsible for the current-reduced coercivity, along with other types of current-induced torques, require further investigation to determine whether they may play a role in CIDM and if it may be able to drive other phenomena such as zero-field switching.[58] While the widefield NV microscope is useful for observing changes in the micromagnetic structure providing real-space insights, complementing NV measurements with techniques that directly probe current-induced torques such as ferromagnetic resonance and harmonic analysis in Hall effect measurements[14] will be necessary to obtain a fuller picture.

ACKNOWLEDGMENTS

This work was supported by the Australian Research Council (ARC) through grants CE170100012, CE170100039, and FT200100073. The work was performed in part at the RMIT Micro Nano Research Facility (MNRF) in the Victorian Node of the Australian National Fabrication Facility (ANFF) and the RMIT Microscopy and Microanalysis Facility (RMMF). I.O.R. and A.J.H. are supported by an Australian Government Research Training Program Scholarship. S.C.S gratefully acknowledges the support of an Ernst and Grace Matthaei scholarship.

* jean-philippe.tetienne@rmit.edu.au

[1] D. L. Cortie, G. L. Causer, K. C. Rule, H. Fritzsche, W. Kreuzpaintner, and F. Klose, Advanced Functional Materials **30**, 1901414 (2020).
[2] W. Li, X. Qian, and J. Li, Nature Reviews Materials **6**, 829 (2021).
[3] H. Kurebayashi, J. H. Garcia, S. Khan, J. Sinova, and S. Roche, Nature Reviews Physics **4**, 150 (2022).
[4] M. Gibertini, M. Koperski, A. F. Morpurgo, and K. S. Novoselov, Nature Nanotechnology **14**, 408 (2019).
[5] C. Gong and X. Zhang, Science **363**, eaav4450 (2019).
[6] D. R. Klein, D. MacNeill, J. L. Lado, D. Soriano, E. Navarro-Moratalla, K. Watanabe, T. Taniguchi, S. Manni, P. Canfield, J. Fernández-Rossier, and P. Jarillo-Herrero, Science **360**, 1218 (2018).
[7] Z. Wang, D. Sapkota, T. Taniguchi, K. Watanabe, D. Mandrus, and A. F. Morpurgo, Nano Letters **18**, 4303 (2018).
[8] S. Albarakati, C. Tan, Z.-j. Chen, J. G. Partridge, G. Zheng, L. Farrar, E. L. H. Mayes, M. R. Field, C. Lee, Y. Wang, Y. Xiong, M. Tian, F. Xiang, A. R. Hamilton, O. A. Tretiakov, D. Culcer, Y.-j. Zhao, and L. Wang, Science Advances **5**, eaaw0409 (2019).
[9] K. Zhang, S. Han, Y. Lee, M. J. Coak, J. Kim, I. Hwang, S. Son, J. Shin, M. Lim, D. Jo, K. Kim, D. Kim, H. Lee, and J. Park, Advanced Materials **33**, 2004110 (2021).
[10] K. Zhang, Y. Lee, M. J. Coak, J. Kim, S. Son, I. Hwang, D. Ko, Y. Oh, I. Jeon, D. Kim, C. Zeng, H. Lee, and J. Park, Advanced Functional Materials **31**, 2105992 (2021).
[11] J. F. Sierra, J. Fabian, R. K. Kawakami, S. Roche, and S. O. Valenzuela, Nature Nanotechnology **16**, 856 (2021).
[12] X. Lin, W. Yang, K. L. Wang, and W. Zhao, Nature Electronics **2**, 274 (2019).
[13] A. Soumyanarayanan, N. Reyren, A. Fert, and C. Panagopoulos, Nature **539**, 509 (2016).
[14] A. Manchon, J. Železný, I. M. Miron, T. Jungwirth, J. Sinova, A. Thiaville, K. Garello, and P. Gambardella, Reviews of Modern Physics **91**, 035004 (2019).
[15] I. M. Miron, T. Moore, H. Szambolics, L. D. Buda-Prejbeanu, S. Auffret, B. Rodmacq, S. Pizzini, J. Vogel, M. Bonfim, A. Schuhl, and G. Gaudin, Nature Materials **10**, 419 (2011).
[16] S. Emori, U. Bauer, S.-M. Ahn, E. Martinez, and G. S. D. Beach, Nature Materials **12**, 611 (2013).
[17] K.-S. Ryu, L. Thomas, S.-H. Yang, and S. Parkin, Nature Nanotechnology **8**, 527 (2013).
[18] A. Fert, N. Reyren, and V. Cros, Nature Reviews Materials **2**, 17031 (2017).

[19] W. Niu, Z. Cao, Y. Wang, Z. Wu, X. Zhang, W. Han, L. Wei, L. Wang, Y. Xu, Y. Zou, L. He, and Y. Pu, Physical Review B **104**, 125429 (2021).

[20] H. Yang, S. O. Valenzuela, M. Chshiev, S. Couet, B. Dieny, B. Dlubak, A. Fert, K. Garello, M. Jamet, D.-E. Jeong, K. Lee, T. Lee, M.-B. Martin, G. S. Kar, P. Sénéor, H.-J. Shin, and S. Roche, Nature **606**, 663 (2022).

[21] M. Alghamdi, M. Lohmann, J. Li, P. R. Jothi, Q. Shao, M. Aldosary, T. Su, B. P. T. Fokwa, and J. Shi, Nano Letters **19**, 4400 (2019).

[22] X. Wang, J. Tang, X. Xia, C. He, J. Zhang, Y. Liu, C. Wan, C. Fang, C. Guo, W. Yang, Y. Guang, X. Zhang, H. Xu, J. Wei, M. Liao, X. Lu, J. Feng, X. Li, Y. Peng, H. Wei, R. Yang, D. Shi, X. Zhang, Z. Han, Z. Zhang, G. Zhang, G. Yu, and X. Han, Science Advances **5**, eaaw8904 (2019).

[23] V. Gupta, T. M. Cham, G. M. Stiehl, A. Bose, J. A. Mittelstaedt, K. Kang, S. Jiang, K. F. Mak, J. Shan, R. A. Buhrman, and D. C. Ralph, Nano Letters **20**, 7482 (2020).

[24] I. Shin, W. J. Cho, E. An, S. Park, H. Jeong, S. Jang, W. J. Baek, S. Y. Park, D. Yang, J. H. Seo, G. Kim, M. N. Ali, S. Choi, H. Lee, J. S. Kim, S. D. Kim, and G. Lee, Advanced Materials **34**, 2101730 (2022).

[25] D. Abdul-Wahab, E. Iacocca, R. F. L. Evans, A. Bedoya-Pinto, S. Parkin, K. S. Novoselov, and E. J. G. Santos, Applied Physics Reviews **8**, 041411 (2021).

[26] K. F. Mak, J. Shan, and D. C. Ralph, Nature Reviews Physics **1**, 646 (2019).

[27] L. Thiel, Z. Wang, M. A. Tschudin, D. Rohner, I. Gutiérrez-Lezama, N. Ubrig, M. Gibertini, E. Giannini, A. F. Morpurgo, and P. Maletinsky, Science **364**, 973 (2019).

[28] E. V. Levine, M. J. Turner, P. Kehayias, C. A. Hart, N. Langellier, R. Trubko, D. R. Glenn, R. R. Fu, and R. L. Walsworth, Nanophotonics **8**, 1945 (2019).

[29] S. C. Scholten, A. J. Healey, I. O. Robertson, G. J. Abrahams, D. A. Broadway, and J.-P. Tetienne, Journal of Applied Physics **130**, 150902 (2021).

[30] D. A. Broadway, S. C. Scholten, C. Tan, N. Dontschuk, S. E. Lillie, B. C. Johnson, G. Zheng, Z. Wang, A. R. Oganov, S. Tian, C. Li, H. Lei, L. Wang, L. C. L. Hollenberg, and J. Tetienne, Advanced Materials **32**, 2003314 (2020).

[31] N. J. McLaughlin, H. Wang, M. Huang, E. Lee-Wong, L. Hu, H. Lu, G. Q. Yan, G. Gu, C. Wu, Y.-Z. You, and C. R. Du, Nano Letters **21**, 7277 (2021).

[32] H. Chen, S. Asif, M. Whalen, J. Támara-Isaza, B. Luetke, Y. Wang, X. Wang, M. Ayako, S. Lamsal, A. F. May, M. A. McGuire, C. Chakraborty, J. Q. Xiao, and M. J. H. Ku, 2D Materials **9**, 025017 (2022).

[33] G. Q. Yan, S. Li, H. Lu, M. Huang, Y. Xiao, L. Wernert, J. A. Brock, E. E. Fullerton, H. Chen, H. Wang, and C. R. Du, Advanced Materials , 2200327 (2022).

[34] H.-J. Deiseroth, K. Aleksandrov, C. Reiner, L. Kienle, and R. K. Kremer, European Journal of Inorganic Chemistry **2006**, 1561 (2006).

[35] C. Tan, J. Lee, S.-g. Jung, T. Park, S. Albarakati, J. Partridge, M. R. Field, D. G. McCulloch, L. Wang, and C. Lee, Nature Communications **9**, 1554 (2018).

[36] Z. Fei, B. Huang, P. Malinowski, W. Wang, T. Song, J. Sanchez, W. Yao, D. Xiao, X. Zhu, A. F. May, W. Wu, D. H. Cobden, J.-h. Chu, and X. Xu, Nature Materials **17**, 778 (2018).

[37] Y. Deng, Y. Yu, Y. Song, J. Zhang, N. Z. Wang, Z. Sun, Y. Yi, Y. Z. Wu, S. Wu, J. Zhu, J. Wang, X. H. Chen, and Y. Zhang, Nature **563**, 94 (2018).

[38] K. Kim, J. Seo, E. Lee, K.-T. Ko, B. S. Kim, B. G. Jang, J. M. Ok, J. Lee, Y. J. Jo, W. Kang, J. H. Shim, C. Kim, H. W. Yeom, B. Il Min, B.-J. Yang, and J. S. Kim, Nature Materials **17**, 794 (2018).

[39] B. Ding, Z. Li, G. Xu, H. Li, Z. Hou, E. Liu, X. Xi, F. Xu, Y. Yao, and W. Wang, Nano Letters **20**, 868 (2020).

[40] H. Wang, C. Wang, Z.-A. Li, H. Tian, Y. Shi, H. Yang, and J. Li, Applied Physics Letters **116**, 192403 (2020).

[41] A. Chakraborty, A. K. Srivastava, A. K. Srivastava, A. K. Srivastava, K. Mohseni, K. Mohseni, H. Deniz, H. Deniz, B. K. Hazra, B. K. Hazra, P. Sessi, I. Kostanovskiy, T. Ma, H. L. Meyerheim, and S. S. P. Parkin, Advanced Materials **34**, 2108637 (2022).

[42] T.-E. Park, L. Peng, J. Liang, A. Hallal, F. S. Yasin, X. Zhang, K. M. Song, S. J. Kim, K. Kim, M. Weigand, G. Schütz, S. Finizio, J. Raabe, K. Garcia, J. Xia, Y. Zhou, M. Ezawa, X. Liu, J. Chang, H. C. Koo, Y. D. Kim, M. Chshiev, A. Fert, H. Yang, X. Yu, and S. Woo, Physical Review B **103**, 104410 (2021).

[43] Ø. Johansen, V. Risinggård, A. Sudbø, J. Linder, and A. Brataas, Physical Review Letters **122**, 217203 (2019).

[44] F. Martin, K. Lee, M. Schmitt, A. Liedtke, A. Shahee, H. T. Simensen, T. Scholz, T. G. Saunderson, D. Go, M. Gradhand, Y. Mokrousov, T. Denneulin, A. Kovács, B. Lotsch, A. Brataas, and M. Kläui, Preprint , arXiv:2107.09420 (2021).

[45] M. W. Doherty, N. B. Manson, P. Delaney, F. Jelezko, J. Wrachtrup, and L. C. Hollenberg, Physics Reports **528**, 1 (2013).

[46] L. Rondin, J.-P. Tetienne, T. Hingant, J.-F. Roch, P. Maletinsky, and V. Jacques, Reports on Progress in Physics **77**, 056503 (2014).

[47] F. Casola, T. van der Sar, and A. Yacoby, Nature Reviews Materials **3**, 17088 (2018).

[48] S. E. Lillie, D. A. Broadway, N. Dontschuk, S. C. Scholten, B. C. Johnson, S. Wolf, S. Rachel, L. C. L. Hollenberg, and J.-P. Tetienne, Nano Letters **20**, 1855 (2020).

[49] D. A. Broadway, S. E. Lillie, S. C. Scholten, D. Rohner, N. Dontschuk, P. Maletinsky, J.-P. Tetienne, and L. C. L. Hollenberg, Physical Review Applied **14**, 024076 (2020).

[50] N. H. D. Khang, Y. Ueda, and P. N. Hai, Nature Materials **17**, 808 (2018).

[51] K.-J. Kim, R. Hiramatsu, T. Koyama, K. Ueda, Y. Yoshimura, D. Chiba, K. Kobayashi, Y. Nakatani, S. Fukami, M. Yamanouchi, H. Ohno, H. Kohno, G. Tatara, and T. Ono, Nature Communications **4**, 2011 (2013).

[52] S. H. Yang, K. S. Ryu, and S. Parkin, Nature Nanotechnology **10**, 221 (2015).

[53] S. Laref, K.-W. Kim, and A. Manchon, Physical Review B **102**, 060402 (2020).

[54] I. A. Ado, G. Rakhmanova, D. A. Zezyulin, I. Iorsh, and M. Titov, Preprint , arXiv:2105.14495 (2021).

[55] T. G. Saunderson, D. Go, S. Blügel, M. Kläui, and Y. Mokrousov, Preprint , arXiv:2204.13052 (2022).

[56] H. Wang, Y. Liu, P. Wu, W. Hou, Y. Jiang, X. Li, C. Pandey, D. Chen, Q. Yang, H. Wang, D. Wei, N. Lei, W. Kang, L. Wen, T. Nie, W. Zhao, and K. L. Wang, ACS Nano **14**, 10045 (2020).

[57] G. K. R. Nair, Z. Zhang, F. Hou, A. Abdelaziem, X. Xu, S. W. Q. Yang, N. Zhang, W. Li, C. Zhu, Y. Wu, H. Weiling, L. Kang, T. Salim, J. Zhou, L. Ke, J. Lin, X. Li, W. Gao, and Z. Liu, Nano Research **15**, 457 (2022).

[58] L. Liu, C. Zhou, X. Shu, C. Li, T. Zhao, W. Lin, J. Deng, Q. Xie, S. Chen, J. Zhou, R. Guo, H. Wang, J. Yu, S. Shi, P. Yang, S. Pennycook, A. Manchon, and J. Chen, Nature Nanotechnology **16**, 277 (2021).